
Article:
Toperesu, PM, Kale, GM orcid.org/0000-0002-3021-5905, Daji, J et al. (2 more authors) (2021) Static and dynamic corrosion behavior of SnO2-doped AZS slip cast refractory in SLS glass. International Journal of Applied Ceramic Technology. ISSN 1546-542X

https://doi.org/10.1111/ijac.13882

Static & Dynamic Corrosion Behaviour of SnO_2 doped AZS slip cast refractory in SLS glass.

Phillip Masimba Toperesu [a,b], Girish M. Kale [a,*], Jafar Daji [b], David E Parkinson [b], Simon Parkinson [b]

[a] School of Chemical and Process Engineering, University of Leeds, Leeds LS2 9JT, U.K.
[b] Parkinson-Spencer Refractories Ltd, Halifax HX3 6SX, U.K.

*Author for all correspondences: g.m.kale@leeds.ac.uk (E); 0044-113-3432805 (T)

Abstract

The corrosion behaviour of a Tin IV Oxide doped AZS - refractory; subject to static and dynamic corrosion testing at 1370˚C in soda-lime-silica glass was studied considering the effect of the microstructural features on corrosion. The refractory was synthesised by slip cast methods through reaction sintering of alumina and zircon raw materials using SnO_2 as a sintering agent. SnO_2 had a considerable influence in the enhanced alumina/zircon reaction sintering and the subsequent evolved microstructures of an interlocked $Zr_{(1-x)}Sn_{(x)}O_2$ solid solution reinforced alumina-mullite composite. The process kinetics of the refractory corrosion followed reasonably well the predicted dependence on the square root of angular velocity under forced convection corrosion. Glass chemical corrosion and erosion of the refractory, under static and dynamic glass conditions respectively, revealed the $Zr_{(1-x)}Sn_{(x)}O_2$ solid solution rich mullite matrix as providing the most corrosion resistance and glass compatibility.

Keywords: Glass corrosion; Tin IV Oxide; alumina, $Zr_{(1-x)}Sn_{(x)}O_2$ solid solution, Refractories.

Funding Sources: This research did not receive any specific grant from funding agencies in the public, commercial, or not-for-profit sectors.

1 Introduction

Production of Soda-lime-silica (SLS) container glasses is commercially done in continuous glass furnaces; principally made up of three sections – a melting tank, distributor and the forehearth.[1,2] Service temperatures at the working hot-end of the glassworks range from 1500 – 1550 °C in the melting tanks; down to 1350 – 1450 ˚C in the distributor and 1100 – 1350 °C in

the forehearth where glass is homogenized and refined before further processing in the forming machines.[1,3] The expected service life of glass furnace linings has improved over the years to >10 years of continuous service. However, this is normally limited as a result of thermal shock failures and or high temperature corrosion of the refractories in an expected but albeit expensive occurrence for glass manufacturers.[3-5] An estimated operational impact cost from these occurrences of about £9M ($10M) is spread over shut-down periods; virgin materials, tearing of worn refractories, reconstruction and subsequent losses in production.[5-6] Additional production losses are also encountered from extensive corrosion of forehearth consumable refractories; known in the industry as expendables, that are utilised for glass homogenisation and gob forming applications such as stirrers, spouts, tubes, plungers and orifice rings;.[5,6] The service life of these expendable parts range from 3 – 12 months depending upon glass composition, furnace throughput and service temperatures.[4-6]

For container glass manufacturing, refractories from the Al_2O_3-ZrO_2-SiO_2 (AZS) system are the choice of materials used in both the glass tanks and forehearth glass contact applications. Fused cast AZS are readily used in the glass tank sections, while sintered/bonded AZS refractories are used in the forehearth and distributor sections.[2-7] Cr-type bonded AZS refractories also find much application in the forehearth and working end sections; due to the unusually low solubility of chromium oxide in siliceous glass melt, - although with risks of glass colouration and possible formation of carcinogenic hexavalent Cr (Cr^{6+}) at higher oxygen potentials and process temepratures.[2-8] Amongst non-colouring oxides, SnO_2 presents the lowest solubility in SLS and Borosilicate glasses with the order of solubility reported as; $SiO_2 > Al_2O_3 > ZrO_2 > SnO_2 > Cr_2O_3$.[9]

The corrosion of AZS and Cr-AZS refractories in most types of glass melts such as SLS,[6-10] Lead crystal,[11-14] Borosilicate,[15,16,] and Calcium Alumina Silicate (CAS)[7,16-18] glasses; has been widely reported, as has been their corrosion mechanisms.[5-19] However; in our literature review, very little has been reported for the SnO_2-AZS system in glass melts. From these studies,[5-19] it has been

shown that many key factors such as composition and phase assemblies of a refractory brick; its texture – i.e., grain sizes, porosity; and their distribution, are key factors that contribute to the corrosion resistance of a refractory material. Furthermore, studies of "post-corrosion" profiles reveals the SEM microstructural features highlighting preferential slag attacks of refractory grains/matrix, and or of a passivating reaction layer at the "SLS glass//refractory" interfaces with ZrO_2 crystals within an alumina-silicate glassy matrix.[5-19] Some of these post-corrosion profile SEM microstructural features have been regarded as evident sites of corrosion resistance improvements from zircon and zirconia additions to the refractory.[6-10] The corrosion mechanism of a zirconia containing AZS refractory was attributed to dissolution and mass transport of zirconia grains into the bulk melt.[5-19]

It is also known that a change of refractory design is an additional possible way of improving the wear/dissolution rate of refractory grains/matrix in glass melts. Authors of this current study demonstrated in a previous study ,[20] the effects of SnO_2 in producing a dense slip cast refractory with a SnO_2-ZrO_2 solid solution reinforced and interlocked acicular mullite microstructure.[20] In the study, the authors also briefly demonstrated the reduced solubility potential of $Zr_{(1-x)}Sn_{(x)}O_2$ solid solution grains in SLS glass and with it the potential improved corrosion resistance of the refractory in SLS glass.[20] Therefore, for this study, the authors are looking at the corrosion/erosion behaviour in SLS glass of the $Zr_{(1-x)}Sn_{(x)}O_2$ solid solution reinforced alumina-mullite refractory; herein known as AZS-T1.

2 Experimental Procedures

In this study, the corrosion behaviour and corrosion resistance of AZS-T1; an optimised $Zr_{(1-x)}Sn_{(x)}O_2$ solid solution reinforced alumina-mullite refractory brick, in contact with SLS glass were investigated under both isothermal static and dynamic corrosion test conditions of 1370 ˚C for 72hr. The crucible/cup test method was used for the static corrosion test, while the rotary finger test was used for dynamic corrosion tests, following a variant of the ASTM C-621 method.

The particle packing optimisation and synthesis of the SnO_2 doped AZS refractory; AZS-T1, is covered in detail in our previous study.[20]

2.1 Materials

Table 1 shows the chemical, mineralogical composition, and the physical material properties of the AZS-T1 refractory; sintered and consolidated at 1550 ˚C, which was used for this study.

Table 1: Material property data of refractory AZS-T1 used in this study.

Crushed SLS cullet; supplied by GTS-Ltd, Sheffield was used in the high temperature corrosion studies as the corroding medium. The typical chemical composition of the glass is provided in table 2.

Table 2: Chemical composition of SLS glass cullet that was used as a corroding medium for this study.

2.2 Static glass corrosion tests

For isothermal static glass corrosion, the crucible/cup samples were made by slip-casting an AZS-T1 slip into four 100mm x 100mm gypsum moulds with a 25 mm diameter x 25 mm depth recess cavity in the middle. The green casts were demoulded from the gypsum moulds after 24hrs and then dried in an electric oven for 5hrs before sintering at 1550 ˚C for 1hr in an electric lab furnace (Nabertherm). For corrosion testing, 25g of SLS glass cullet was placed into each of the sintered corrosion cup samples/crucibles. The samples were covered with an alumina cover, placed in an electric furnace and isothermal glass corrosion testing conducted at 1370˚C for 72 hrs according to the ASTM C621 – 09 methods. Following corrosion testing, the cup samples were sectioned across the mid-point and examined for further study of their corrosion profiles and characteristics.

2.3 Dynamic glass corrosion tests

For dynamic corrosion testing, the widely practised “rotary finger test/merry-go-round” method was implemented, where refractory coupons/finger samples are immersed in a glass melt bath and rotated to simulate the forced convection corrosion of refractories in industry.

100mm length x 15mm diameter - cylindrical finger specimen samples of the AZS-T1 refractory were core drilled from a sintered AZS-T1 block. For comparison and as reference materials, finger specimen samples of two commercial refractories from the AZS and AZM system, widely used in glass industries were also core drilled from AZS and AZM refractory blocks. An alumina crucible was used as a melting crucible for the SLS glass. A bespoke in-house, designed, and fabricated motorised equipment with a top loading furnace (Lenton Thermal Designs Ltd, Market Harborough, UK) was employed for high temperature dynamic corrosion testing. The equipment; shown in figure 1, consist of an adjustable frame connected to a ceramic sample holder attached to a ceramic shaft and a winch which is used to lower and immerse the samples into the glass melt bath as well as lift them up after the experiment. The rotation speed was controlled by a motor (Parvalux Electric Motor Ltd, Dorset, UK), which was mounted on the adjustable sample holder frame. The isothermal dynamic corrosion tests were conducted as a function of rotation speed at standard test temperature of 1370 ˚C. The rotation speeds used were 0; 1.5; and 5.5 rpm, which corresponds to a linear molten glass flow rate of 0-, 188- and 688-mm min^{-1} respectively. The standard glass flow rate in the glass industry is typically 180 mm/min.[2,5,6] The duration for each corrosion test run was 72hr.

Figure 1: Set up of the dynamic glass corrosion test equipment.

- **(A) Part of the bespoke in-house made, designed and fabricated motorised contraption with a top loading furnace used for the dynamic corrosion test.**
- **(B) Ceramic shaft with sample holder lowered into alumina crucible with crushed SLS cullet prior to corrosion testing.**
- **(C) Part of the dynamic corrosion test rig showing samples being immersed in molten SLS glass at 1370 ˚C during dynamic corrosion test.**
- **(D) Ceramic sample holder with finger samples after corrosion testing.**

The "before and after" material loss method was used to evaluate the corrosion rate and corrosion index of the finger samples under dynamic conditions. The diameters of the melt or glass-line regions of the test samples before and after the corrosion tests were measured by an optical micrometer and the materials loss calculated. Following the glass industry standard, the corrosion index of refractories was calculated according to equation 1 where, $\boldsymbol{D_i}$ and $\boldsymbol{D_r}$ denotes

the initial and remaining diameter of the test piece, and $\boldsymbol{A}$ and $\boldsymbol{R}$ are the test piece and reference refractory sample (AZS or AZM) piece, respectively.

$$\text{Corrosion index for test sample} = \frac{\boldsymbol{A}\rightarrow(\boldsymbol{D_i} - \boldsymbol{D_r})^2}{\boldsymbol{R}\rightarrow(\boldsymbol{D_i} - \boldsymbol{D_r})^2} \quad (1)$$

2.4 Analysis

Chemical and mineralogical analysis of the sintered refractory products was conducted by XRF and the XRD Bruker D8 X-ray diffractometer (Oxford UNITS). A Carl Zeiss EVO MA15 variable pressure W. (tungsten tip) SEM (Oxford Instruments) together with Oxford Instruments Aztec Energy EDX system with 80mm X-Max SDD detector- secondary and backscattered imaging was used to analyse the refractory/glass interface and corrosion profiles after both static and dynamic glass corrosion.

3 Results & Discussions

3.1 AZS-T1 Refractory Material

From the material property and chemical composition of the AZS-T1 refractory, shown in table 1, AZS-T1 is classified as a dense and low porosity high alumina refractory. Typical porosity values of sintered AZS refractories are about 20 %.[1,4,5,9] XRD pattern of the virgin AZS-T1 refractory, pre-glass corrosion testing; (i.e. AZS-T1 sintered at 1550 ˚C for 1hr), is shown in figure 2.

The pattern shows the refractory as consisting of mainly $Zr_{(1-x)}Sn_{(x)}O_2$ ss (zirconia – tin oxide, solid solution), alumina and mullite mineral phases. Table 1; from quantitative XRD and Rietveld analysis, shows the three mineral phases as the major phases (> 25 wt. %) and as also consisting of a minor (6.6 wt. %) amorphous phase.

Figure 2: XRD pattern of refractory AZS-T1 refractory sintered at 1550C.
A = α-Al_2O_3; M = $Al_6Si_2O_{13}$; Zr-Sn = $Zr_{0.93}Sn_{0.07}O_2$ (monoclinic); Zr-$_{(t)}$ = ZrO_2 (tetragonal)

Figure 3 shows the microstructure of the sintered AZS-T1 refractory. From microstructural analysis, SEM micrographs in figure 3a reveal the AZS-T1 microstructure as consisting of tabular alumina aggregates, reinforced in a $Zr_{(1-x)}Sn_{(x)}O_2$ ss and mullite matrix. Further SEM analysis of the matrix shows a homogenous dispersion of interlocked $Zr_{(1-x)}Sn_{(x)}O_2$ ss crystals within a spatial mullite matrix arrangement of acicular tertiary (MIII) mullite to a granular primary MI mullite grains, fig 3b and 3c.

The tertiary acicular MIII mullite occurs near agglomerates of $Zr_{(1-x)}Sn_{(x)}O_2$ crystals, from the dissociated zircon relic grains, with EDX semi-quantitative analysis revealing the Al_2O_3:SiO_2 ratios of MIII and MI mullite to be 77.8**:**22.2 wt. % (i.e., 2:1 mullite) and 72.1**:**27.9 wt. % (- a near stoichiometric 3:2 mullite); respectively. The 2:1 acicular grown mullite was seen to also contain minor impurities of up to 3.1 wt. % SnO_2 and 0.4 wt. % ZrO_2. Therefore, the microstructure of the AZS-T1 refractory is one of a monoclinic $Zr_{(1-x)}Sn_{(x)}O_2$ reinforced 2:1 and 3:2 mullite and alumina composite with some minor tetragonal $Zr_{(1-x)}Sn_{(x)}O_2$ phase.

Figure 3: SEM micrographs showing evolved microstructure of the AZS-T1 sintered at 1550˚C.

- **a) Typical overall microstructure of AZS-T1 consisting of alumina aggregate grains in a $Zr_{(1-x)}Sn_{(x)}O_2$ solid solution (ss) rich mullite matrix.**
- **b) Composition of AZS-T1 matrix, showing evolved primary (MI), and secondary (MII) and tertiary acicular (MIII) mullite grains reinforced by $Zr_{(1-x)}Sn_{(x)}O_2$ solid solution grains.**
- **c) Magnified region of the matrix showing dispersion of intragranular and intergranular $Zr_{(1-x)}Sn_{(x)}O_2$ solid solution grains within mullite matrix.**

3.2 SLS glass/Refractory compatibility – Static Glass Corrosion Test

In glass making, the dissolution/corrosion and erosion of the refractory in contact with moving molten glass determines its service life span while the defect potential of a refractory in producing glass defects such as stones, blisters/seeds/bubbles, and cords (local glass of different composition and refractive index) will determine the quality of the glass. Therefore, for the first section of this study the refractory-glass compatibility of the AZS-T1 refractory and its defect forming potential were evaluated from the static glass corrosion tests.

Figure 4; (a) - (c), shows a sectioned static corrosion cup sample, a finger sample specimen of the AZS-T1 refractory and a reference commercial AZS refractory after static corrosion testing,

respectively. While figure 4d shows a schematic of surface tension driven glass-line cut mechanism.

Figure 4: Post mortem refractory samples from a static SLS glass corrosion test at 1370 C for 72hrs.

- **a) A sectioned AZS-T1 static corrosion cup/crucible sample showing refractory, glass, and the glass/refractory interface.**
- **b) AZS-T1 finger sample after static corrosion testing in SLS glass.**
- **c) Commercial AZS finger sample, as reference sample after static corrosion testing in SLS glass.**
- **d) Schematic diagram of a typical refractory-glass melt interaction showing time dependent sequence of melt/glass line corrosion cut. Taken from [3].**

Preliminary visual analysis of the samples reveals a smooth, clean glass/refractory interface and corrosion profiles that do not show any noticeable corrosion of the AZS-T1 refractory by SLS glass under the test conditions (figure 4a and 4b). There was also very limited cracking (micro or macro) in the samples and no visible glass penetration in the virgin refractory. This highlighted good thermal stress/shock properties of the low porosity refractory coming from the interlocked $Zr_{(1-x)}Sn_{(x)}O_2$ reinforced mullite matrix. It also ruled out wear of the refractory due to mechanical weakness or spalling of the refractory as a result of any possible new phases evolving from glass infiltration and interaction within the refractory matrix. From figure 4, it can be seen that both the AZS-T1 refractory cup and finger samples, do not exhibit any glass-line corrosion and or any tapered corrosion profiles beneath the glass-line, characteristic of free upward or downward corrosion convection currents associated with either alumina or zirconia dissolution of an AZS refractory in a lead containing glass or SLS glass system, respectively.

It is known that these distinct free convection corrosion melt-line cut/neck profiles at or near the glass line are a result of surface tension and density gradients between the bulk glass and glass containing dissolved refractory near the interface and air/glass/refractory - triple face boundary.[3,6,16] It is also known that alumina and zirconia act to increase the surface tension and density of SLS glass upon dissolution of the refractory.[3,6,7,16] Therefore, this clearly indicates a good refractory/glass compatibility and an excellent corrosion/dissolution resistance of the AZS-T1 refractory to SLS glass at the test temperature. SEM and EDX analysis of the SLS glass/AZS-T1 refractory interface proves this to be the case where figure 5a, shows a smooth clean glass/refractory interface, and elemental mapping highlighting relatively insignificant crossover of the glass constituents into the virgin refractory zone.

A closer examination of the SLS glass and AZS-T1 refractory interface and, the reaction zone, in Figure 5b, shows part of the matrix and alumina aggregate grains in contact with the glass at the interface. Figure 5b further shows that in this reaction zone there is preferential attack of mullite, and alumina grains compared with the $Zr_{(1-x)}Sn_{(x)}O_2$ grains by the glass with minimum or slower corrosion of the $Zr_{(1-x)}Sn_{(x)}O_2$ grains and $Zr_{(1-x)}Sn_{(x)}O_2$ rich matrix.

Figure 5: SEM micrographs and EDX analysis on the interface.

a) SEM elemental mapped SLS glass and AZS-T1 refractory interface showing the elemental distribution of AZS-T1 and SLS glass constituents across the interface.

b) Refractory – Glass Interface of AZS-T1 and SLS glass; showing grains of $Zr_{(1-x)}Sn_{(x)}O_2$ solid solution in chemical equilibrium with the SLS glass.

This is further verified; from table 3, by SEM point/spectrum EDS semi-quantitative analysis of the SLS glass region and adjacent boundary layer, circa 20μm from the interface, which shows more Al^{3+} content (3.1 wt.%) than Zr^{4+} (1.1 wt.%) within the parent SLS glass from the dissolution of the respective refractory phases in contact with the glass. No Sn^{4+} signatures are detected in the glass. However, when comparing similar behaviour of a commercial AZS refractory in contact with molten SLS glass, it can be seen from table 3 that the alumina and zirconia dissolved from the commercial AZS refractory by the SLS glass was by twofold and fivefold more than was dissolved from the AZS-T1 refractory, respectively.

Table 3: Chemical composition of selected point/spectrum of SLS glass and boundary layer near interface with AZS-T1.

As such it is conceivable that; for the commercial, reference AZS refractory, the surface tension gradients and density gradients of the SLS glass are significantly increased leading to the glass-line cut profiles and mechanism highlighted in the schematic in figure 4d. It can therefore be deduced that the relatively slow dissolution of the $Zr_{(1-x)}Sn_{(x)}O_2$ rich matrix of the AZS-T1 refractory; and hence by order, the relatively reduced amount of alumina and zirconia (from $Zr_{(1-x)}Sn_{(x)}O_2$ solid solution grains) dissolved in the SLS glass, in comparison with the commercial AZS refractory explains why for the AZS-T1 refractory, no free convection corrosion glass-line cut/neck profiles occur. Consequently, this shows the enhanced corrosion /dissolution resistance imparted to the matrix of the AZS-T1 refractory by the $Zr(1-x)Sn_{(x)}O_2$ solid solution as

well as some SnO_2 incorporation in the mullite and as such highlights a well-designed refractory in the matrix region.

3.3 Dynamic Corrosion

Under static glass corrosion test conditions at 1370˚C, as described in the previous section it was shown that the AZS-T1 refractory presented excellent chemical compatibility and corrosion resistance against SLS glass. The next step for this study was to study how the refractory would perform under forced convection conditions at the same test temperature of 1370 ˚C for 72h. For reference and comparison of the corrosion index of the refractories, i.e., following the glass industry standard, finger samples taken from two commercial AZS and AZM refractories, were also tested under the same dynamic corrosion test conditions. Figure 6 shows the corroded and eroded, post mortem finger samples of the AZS-T1 refractory after dynamic corrosion testing, where the level of corrosion and erosion was determined

Figure 6 also shows, for comparison and as reference, the two AZS and AZM refractories also tested under similar dynamic corrosion conditions. From figure 6, it can be seen that for the AZS-T1 refractory, unlike the results from the static/free convection corrosion testing, with forced glass convection at play, the onset of glass line corrosion cut profiles on the AZS-T1 refractory occurs and become more pronounced with increasing rotation speed or glass flow rate. The reference AZS and AZSM refractory materials comparatively show more pronounced glass-line corrosion cut profiles with increasing rotation speed than for the AZS-T1refractory under similar dynamic conditions.

Figure 6: Post mortem dynamic corrosion finger samples of the AZS-T1 and two reference commercial refractories, from the AZS and AZM system.

a) AZS-T1 finger samples from corrosion testing in SLS glass at 0, 1.5, 3.5 and 5 rpm
b) Corroded commercial AZS and AZM refractory finger samples, used as reference samples in this study, after dynamic corrosion testing at 5rpm in SLS glass.
c) Comparison of corrosion profiles of the AZS-T1 and commercial AZS and AZM refractories after dynamic corrosion testing at 5rpm in SLS glass.

It is known and has been shown by various studies that the enhanced preferential corrosion of the mineral phases that constitute a refractory; as highlighted in this study - in Figure 5b, is due to the chemical reaction between the mineral phases and primarily Na^{+} cations and Ca^{2+} cations from the SLS glass constituents.[3,4,6,18] Under stagnant or free convection conditions, a boundary layer, δ, is formed. Furthermore, Cooper and Kingery (1964),[16] showed that under forced convection, the process kinetics for the rate of dissolution of refractory is controlled by the mass transport away from the interface and boundary layer into the liquid glass melt which is proportional to the square root of angular velocity, $\omega^{½}$, according to equation 2

$$J = 0.61 \cdot \lambda \cdot D_{\infty}^{2/3} \cdot v_{\infty}^{-1/8} \cdot \omega^{½} \cdot C \qquad (2)$$

With; **λ**, defined as a correction coefficient to account for variable properties; bulk diffusion coefficient – $\mathbf{D}_{\infty}$; viscosity - $\mathbf{v}_{\infty}$; Angular velocity ω; and glass concentration parameter – **C**. A plot of the rate of corrosion of AZS-T1 finger samples as a function of the rotation speed in radians; i.e., the square root of angular velocity is shown in figure 7. The plot shows that the rate of corrosion of AZS-T1 follows reasonably well the predicted dependence on the square root of angular velocity of the forced convection.

Figure 7: Dependence of rate of corrosion of AZS-T1 refractory on the square root of angular velocity.

This means that the corrosion process kinetics for the AZS-T1 refractory is mass transfer dependent under forced convection conditions, similar to other typical AZS and AZM refractories as reported in various studies.[3,6,7,10,12,15,16] Under forced convection, as the melt moves over the refractory at high velocities, the boundary layer thickness, δ, is reduced, and thus the corrosion rate becomes high. The increased refractory and melt line corrosion is because of the synergistic effect of the chemical corrosion/dissolution of the refractory mineral phases at the glass/refractory interface and forced convection erosion/mass transport of the dissolved refractory products boundary layer away from the interface into the bulk molten SLS glass. Therefore, by comparing the post corrosion test profiles of the tested AZS-T1 finger samples with those of the reference , AZS and AZM finger sample materials shown in figure 6, it is easily

seen that the AZS-T1 refractory offers excellent and better corrosion resistant properties in SLS glass than the two well-known and widely used commercial AZS and AZM refractories. This is clearly highlighted in figure 8 when comparing the corrosion index of the tested refractories.

Figure 8: Plot of the corrosion index of AZS-T1 and two commercial AZS and AZM refractories in SLS glass against rotation speed or equivalent glass flow rate at 1370 ˚C

Figure 8 show a plot of the corrosion index of the AZS-T1 and commercial AZS and AZM refractories against the rotation speed or equivalent glass flow rate. From figure 8 , it can be seen that the AZS-T1 refractory offers from twice up to 3 ½ times more corrosion resistant behaviour in SLS glass, with increasing rotation speed/ equivalent glass flow rate than the commercial AZS and AZM refractories under these dynamic test conditions.

SEM microstructural analysis of the corroded and eroded AZS-T1 finger samples that were tested under forced convection or rotation speeds of 3.5 rpm (437.5 mm min^{-1} equivalent glass flow) are shown in figure 9.

Figure 9: SEM micrographs showing corroded and eroded microstructure of the AZS-T1 in SLS glass after dynamic corrosion testing at 3.5 rpm.

a) Microstructure of the AZS-T1 refractory – SLS glass interface.
b) High magnification BSE SEM micrograph of the interface and boundary layer of the AZS-T1/SLS glass interface.

From figure 9a, the interface of the glass/refractory interaction for the AZS-T1 refractory under forced convection corrosion shows some preferential corrosion and erosion of the matrix and exposed alumina aggregates similar to features seen under static or free convection corrosion. Figure 9a, further shows a densified refractory reaction zone of about 300µm from the interface as a result of the SLS glass melt ingress and interaction with the refractory at and beyond the interface.

Figure 9 also further reveals from the texture and porosity of the tabular alumina aggregates that the low porosity of the refractory and interlocked $Zr_{(1-x)}Sn_{(x)}O_2$ rich mullite matrix provides an enhanced corrosion resistance and prevented further ingress of the SLS glass into the refractory zone. EDS semi-quantitative analysis of the SLS glass region and adjacent the

boundary layer, spectrum 37, shown in table 4 reveal that the bulk glass, about 500µm from the interface contains relatively small amounts of Al^{4+} (3.4 wt.%) and Zr^{4+} (0.8 wt.%).

High mag SEM BSE analysis of the interface, figure 9b, reveals small rounded ZrO_2 grains, < 2µm in size; and an alumina rich (15.0 wt. %) glassy phase; spectrum 39. Point-EDS quant analysis of the grain reveals no SnO_2 suggesting that the ZrO_2 had most likely precipitated out from a supersaturated glassy interface/boundary layer on cooling after corrosion testing. The alumina-rich glassy phase at the interface, which makes up the boundary layer, would have been from the mullite contained in the matrix and or dissolved tabular alumina aggregates. No acicular corundum crystals were observed in the glassy phase. This could be attributed to the alumina content not being enough to precipitate in the liquid phase during cooling and attest to the enhanced corrosion resistance properties of the AZS-T1 refractory against SLS glass at the test temperature and dynamic conditions.

Table 4: Chemical composition of selected point/spectrum of SLS glass and boundary layer near interface with AZS-T1 after dynamic corrosion testing at 3.5 rpm.

4 Conclusion

We have shown the corrosion behaviour of AZS-T1; a slip cast refractory from the AZS system doped with SnO_2, in SLS glass under both static/free convection and dynamic /forced convection corrosion at 1370˚C for 72hrs. The corrosion rate or process kinetics of AZS-T1 in SLS glass follows similar trend compared with that of various refractories from the AZS and AZM system, as being mass transport dependent and was proportional to the speed of angular velocity under forced convection. However, AZS-T1 showed excellent corrosion resistant properties of up to 3-fold increase when compared with commercial refractories from the AZS and AZM system that are widely used in the glass industries. Therefore, we strongly believe that AZS-T1 refractory composition exhibits a significant potential of developing in to a commercial refractory for SLS glass making industries.

References

1. Busby, T. S. Progress of glass making refractories. Journal of Non-Crystalline Solids, 26(1-3), pp264–306 (1977).
2. Shelby, J.E., Introduction to Glass Science & Technology. 2nd ed. vol. 2nd. Cambridge: Royal Society of Chemistry. (2005)
3. Burdick V.L. The Corrosive Nature of Molten Glass. In: Pye L.D., Stevens H.J., LaCourse W.C. (eds) Introduction to Glass Science. Springer, Boston, MA. (1972)
4. Vago E, Smith C.E, "The Corrosion of Refractory Materials by Molten Glass," Paper #62, Proc. Seventh International Congress on Glass, Brussels (1965).
5. Parkinson D.E., Feeder and forehearth refractories, Glass Technology 29 (5) pp173–176 (1988)
6. Rigaud M, Landy R.A, eds., Corrosion of Refractories: The Impact of corrosion. FIRE Compendium Series. Goller Verlag. Baden-Baden. (2018).
7. Samaddar B.N, Kingery W.D, Cooper A.R, Jr., "Dissolution in Ceramic Systems: II, Dissolution of Alumina, Mullite, Anorthite and Silica in Calcium Aluminum Silicate Slag," J. Am. Ceram. Soc., 47(5), pp249–254 (1964).
8. Jacob, K.T., Kale, G.M. and Abraham, K.P.: Electrochemical Determination of Gibbs Energies of Formation of Calcium Chromite and Chromate. J. Electrochem. Soc. (U.S.A.), 139, 517 520 (1992).
9. Manfredo L. J, McNally, R. N. Solubility of Refractory Oxides in Soda Lime Glass. J. Am. Ceram. Soc., 67, pp.155-158 (1984).
10. Aksel C. The microstructural features of an alumina–mullite–zirconia refractory material corroded by molten glass. Ceramics International, 29, (3) pp305-309 (2003).
11. Hilger, J.P., Babel, D., Prioul, N, Fissolo, A. Corrosion of AZS and Fireclay Refractories in Contact with Lead Glass. J. Am. Ceram. Soc., 64, pp213-220 (1981).
12. Pavlovskii V.K, Sobolev Yu. S, "Corrosion resistance of refractory oxides in molten high-lead silicate glasses," Steklo Keram. 6, pp7–8 (1991).
13. Rahimi R.A, Ahmadi A, Kakooei S, Sadrnezhaad S.K., Corrosion behaviour of ZrO2–SiO2–Al2O3 refractories in lead silicate glass melts, J. Eur. Ceram. Soc., 31, (5) (2011).
14. Duvierre G, Stertain E, Reber A. Advantages of using high zirconia refractories in lead crystal glass electric furnaces. Glass Technology 34, pp181–186, (1993).
15. Pavlovskii, V.K., Petrov, V.N. & Sobolev, Y.V. Interaction of refractories with a borosilicate glass melt. Glass Ceram 47, 391–393 (1990).
16. Li.H, Cheng J, Tang L. Corrosion of electrocast AZS refractories by CAS glass–ceramics melting. Journal of Non-Crystalline Solids 354, pp1418–23 (2008).
17. Cooper A. R., Jr., Kingery W. D, "Dissolution in Ceramic Systems: I, Molecular Diffusion, Natural Convection and Forced Convection Studies of Sapphire Dissolution in Calcium Aluminum Silicate," J. Am. Ceram. Soc., 47(1), pp37–43 (1964).
18. Reed L, Barrett L. R., "The Slagging of Refractories: I, The Controlling Mechanism in Refractory Corrosion," Trans. Brit. Ceram. Soc., 54, 671 (1955).
19. Kingery W. D., "Corrosion of Refractories by Liquid Melts," Symposium on High Temperatures, Stanford Research Institute pp. 126-132 (1956).
20. Toperesu P.M, Kale G.M, Daji J, Parkinson D.M., Development and evolution of a novel $Zr_{(1-x)}Sn_{(x)}O_2$ toughened alumina-mullite slip cast refractory: Effect of SnO2. J. Eur. Ceram. Soc., 41, (3) pp2134-2144 (2021),

Table 1: Material property data of refractory AZS-T1 used in this study.

Chemical Composition (wt. %)								
Al_2O_3	**SiO_2**	**ZrO_2**	**SnO_2**	***R_2O**	**CaO**	**Fe_2O_3**	**TiO_2**	**Others**
57.8	13.0	24.6	4.3	0.2	0.08	0.06	0.04	<0.02

* $R_2O = Na_2O + K_2O$;

Mineralogical Composition (wt. %)						
α-Al_2O_3	**ZrO_2**	**SiO_2**	**SnO_2**	**Mullite**	**$ZrSiO_4$**	**Amorphous**
38.3	*26.4	-	0.5	27.7	-	6.6

* as $Zr_{(1-x)}Sn_xO_2$ solid solution

Physical Properties			
Bulk Density (Kg m^{-3})	**Apparent Porosity** (%)	**CCS** (MPa)	**HMOR @ 1400 °C** (MPa)
3.41	8.5	163	23.4

Table 2: Chemical composition of SLS glass cullet that was used as a corroding medium for this study.

Chemical Composition (wt. %)						
SiO_2	**CaO**	**Na_2O**	**K_2O**	**MgO**	**Al_2O_3**	***Others**
72.3	11.1	12.9	0.3	2.0	1.2	< 0.4

*Others = trace (TiO_2 + Fe_2O_3 + ZrO_2 + Cr_2O_3 + SO_3)

Table 3: Chemical composition of selected point/spectrum of SLS glass and boundary layer near interface with AZS-T1.

Chemical Composition of glass by Energy dispersive Spectroscopy (EDS) (wt. %)		**O**	**Al**	**Si**	**Zr**	**Sn**	**Ca**	**Na**
Spectrum	Phase							
44	**SLS Glass**, ~ 20µm from the interface	46.7	3.1	33.0	1.1	0	7.4	8.7
45	**AZS-T1**, $Zr_{(1-x)}Sn_{(x)}O_2$ grain in equilibrium with SLS glass by the interface	26.2	0.0	0.9	66.3	5.6	0.0	0.9
Reference AZS	**SLS Glass,** ~ 20µm from the interface with commercial AZS refractory material	46.9	5.8	31.9	4.9	-	5.6	4.9

Table 4: Chemical composition of selected point/spectrum of SLS glass and boundary layer near interface with AZS-T1 after dynamic corrosion testing at 3.5 rpm.

Chemical Composition of glass by Energy	**O**	**Al**	**Si**	**Zr**	**Sn**	**Ca**	**Na**

Dispersive Spectroscopy (EDS) (wt. %)								
Spectrum	Phase							
37	**SLS Glass**, ~ 500µm from the interface	47.4	3.4	34.0	0.8	0.0	7.2	6.8
38	**SLS Glass,** ~ >20µm from the interface with AZS-T1 refractory	46.4	10.7	27.6	1.9	0.5	3.8	8.7
39	**Boundary layer,** ~ <20µm from the interface with AZS-T1 refractory	45.9	15.0	23.7	0.7	0.6	3.2	10.6

Figure 1: Set up of the dynamic glass corrosion test equipment. (A) Part of the bespoke in-house made, designed and fabricated motorised contraption with a top loading furnace used for the dynamic corrosion test. (B) Ceramic shaft with sample holder lowered into alumina crucible with crushed SLS cullet prior to corrosion testing. (C) Part of the dynamic corrosion test rig showing samples being immersed in molten SLS glass at 1370 ˚C during dynamic corrosion test. (F) Ceramic sample holder with finger samples after corrosion testing.

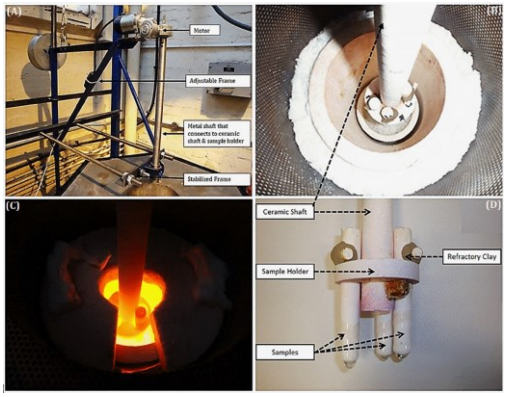

Figure 2: XRD pattern of refractory AZS-T1 refractory sintered at 1550C. A = α-Al_2O_3; M = $Al_6Si_2O_{13}$; Zr-Sn = $Zr_{0.93}Sn_{0.07}O_2$ (monoclinic); Zr-$_{(t)}$ = ZrO_2 (tetragonal).

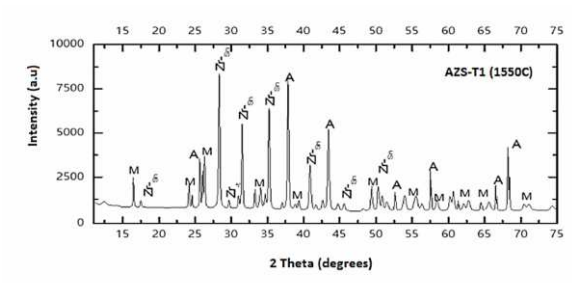

Figure 3: SEM micrographs showing evolved microstructure of the AZS-T1 sintered at 1550˚C. a) Typical overall microstructure of AZS-T1 consisting of alumina aggregate grains in a $Zr_{(1-x)}Sn_{(x)}O_2$ solid solution (ss) rich mullite matrix. b) Composition of AZS-T1 matrix, showing evolved primary (MI), and secondary (MII) and tertiary acicular (MIII) mullite grains reinforced by $Zr_{(1-x)}Sn_{(x)}O_2$ solid solution grains. c) Magnified region of the matrix showing dispersion of intragranular and intergranular $Zr_{(1-x)}Sn_{(x)}O_2$ solid solution grains within mullite matrix.

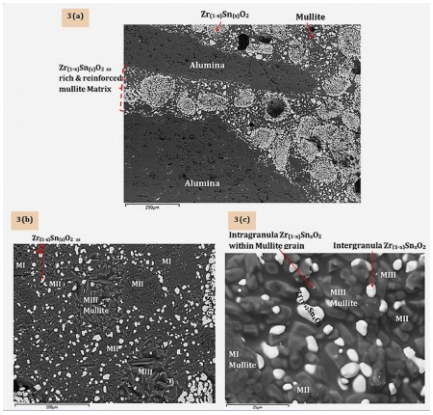

Figure 4: Post mortem refractory samples from a static SLS glass corrosion test at 1370 C for 72hrs. a) A sectioned AZS-T1 static corrosion cup/crucible sample showing refractory, glass, and the glass/refractory interface. b) AZS-T1 finger sample after static corrosion testing in SLS glass. c) Commercial AZS finger sample, as reference sample after static corrosion testing in SLS glass. d) Schematic diagram of a typical refractory-glass melt interaction showing time dependent sequence of melt/glass line corrosion cut. Taken from [3].

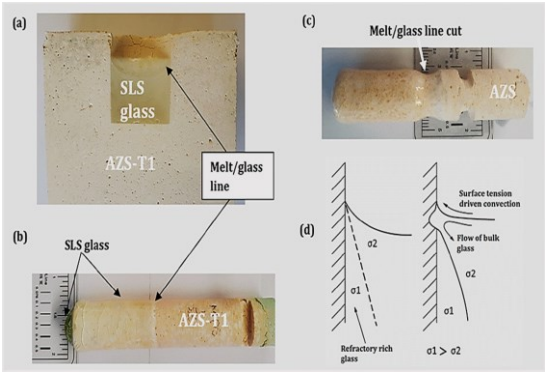

Figure 5: SEM micrographs and EDX analysis on the interface. a) SEM elemental mapped SLS glass and AZS-T1 refractory interface showing the elemental distribution of AZS-T1 and SLS glass constituents across the interface. b) Refractory – Glass Interface of AZS-T1 and SLS glass; showing grains of $Zr_{(1-x)}Sn_{(x)}O_2$ solid solution in chemical equilibrium with the SLS glass.

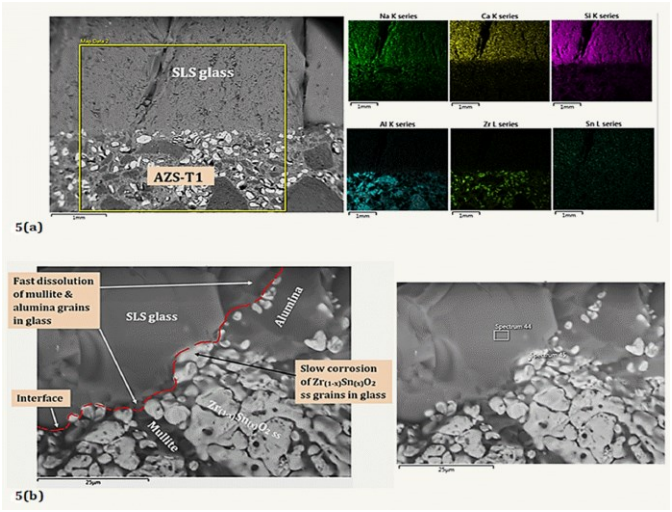

Figure 6: Post mortem dynamic corrosion finger samples of the AZS-T1 and two reference commercial refractories, from the AZS and AZM system. a) AZS-T1 finger samples from corrosion testing in SLS glass at 0, 1.5, 3.5 and 5 rpm. b) Corroded commercial AZS and AZM refractory finger samples, used as reference samples in this study, after dynamic corrosion testing at 5rpm in SLS glass. c) Comparison of corrosion profiles of the AZS-T1 and commercial AZS and AZM refractories after dynamic corrosion testing at 5rpm in SLS glass.

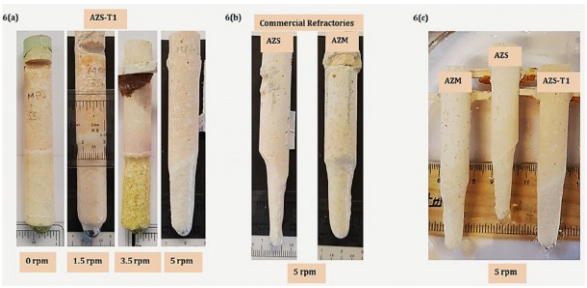

Figure 7: Dependence of rate of corrosion of AZS-T1 refractory on the square root of angular velocity.

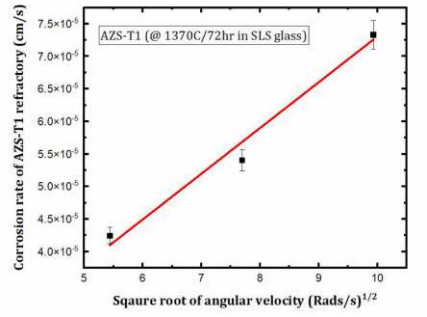

Figure 8: Plot of the corrosion index of AZS-T1 and two commercial AZS and AZM refractories in SLS glass against rotation speed or equivalent glass flow rate at 1370 ˚C

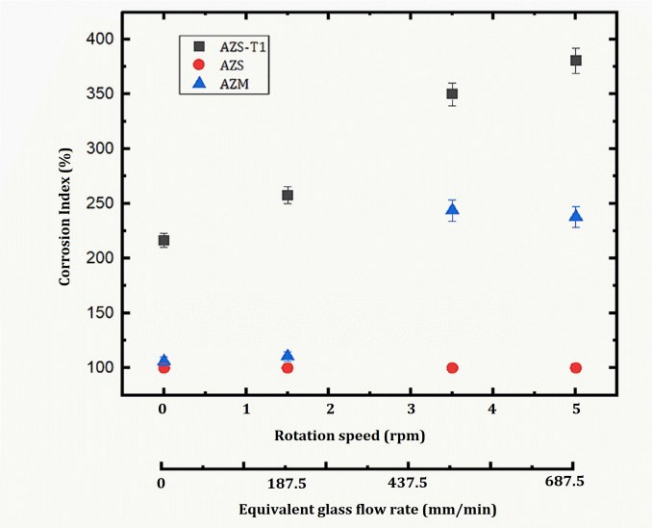

Figure 9: SEM micrographs showing corroded and eroded microstructure of the AZS-T1 in SLS glass after dynamic corrosion testing at 3.5 rpm. a) Microstructure of the AZS-T1 refractory – SLS glass interface. b) High magnification BSE SEM micrograph of the interface and boundary layer of the AZS-T1/SLS glass interface.